Appl Phys B (2010) 99: 433–439
DOI 10.1007/s00340-009-3886-0

Applied Physics B
Lasers and Optics

Coherent phase contrast imaging of THz phonon–polariton tunneling

P. Peier · K.A. Nelson · T. Feurer

Received: 30 September 2009 / Published online: 15 January 2010

Abstract We report on coherent spatiotemporal imaging of single-cycle THz waves in frustrated total internal reflection geometry. Our technique yields images of the spatiotemporal electric field distribution before and after tunneling through an air gap in between two $LiNbO_3$ crystals. Measurements of the reflected and the transmitted THz waveforms for different tunnel distances allow for a direct comparison with results from a causal linear dispersion theory and excellent agreement is found.

1 Introduction

Tunneling is an omnipresent phenomenon in quantum physics [1] and describes, for example, a particle passing through a potential barrier, a process which cannot be explained by classical means [2]. Tunneling is also known in classical optics, most prominently in frustrated total internal reflection [3] but also in several other cases, such as propagation through photonic bandgap structures or through waveguides below the cutoff frequency [4]. Frustrated total internal reflection was first considered by Hall [5] and was further investigated in the infrared regime [6] as well as in the optical regime [7]. In the past, tunneling was often linked to super-luminal wave propagation [8–10] and it was unclear whether causality is violated [11] which would have far reaching consequences. In all cases, however, super-luminal wave propagation was unmasked to be apparent only; essential for a correct analysis is to consider at least two spatial dimensions [12–14]. When electromagnetic pulses rather than plane waves impinge on an interface separating two different dielectric media, one has to distinguish between phase and group velocity and to bear in mind that light pulses are subject to strong reshaping as they pass through the tunneling barrier. Such a situation is investigated best with techniques that allow for coherent field measurements, so that access to the amplitude and phase of the field after tunneling is granted. These techniques are readily available in the microwave and the THz spectral regions. Several experiments in the microwave region report on accurate amplitude and phase measurements of the transmitted signal, for example after tunneling through a waveguide [15]. Mugnai and coworkers derived a detailed analytic model for tunneling through a barrier, compared it to microwave experiments and found good agreement [16]. With the advancements in coherent THz pulse generation and detection it became possible to investigate the tunneling process at higher frequencies. Wynne and coworkers and also Reiten and coworkers have analyzed tunneling of pulsed THz radiation in frustrated total internal reflection and in waveguides [17–19]. The latter group has shown that earlier claims on non-causal light propagation relied on improper assignment of a ray path through the tunnel barrier and that a proper description based on linear dispersion theory can be formulated which obeys causality.

Here, we investigate tunneling of THz single-cycle waves through a potential barrier. Phonon–polaritons are generated through optical rectification of a short visible laser pulse in a suitable nonlinear crystal [20–22], such as $LiNbO_3$, and are admixtures of electromagnetic radiation and lattice phonons. They propagate through the material at almost light-like velocities and may be detected at any given time after excita-

P. Peier (✉) · T. Feurer
Institute of Applied Physics, University of Bern, Sidlerstrasse 5, CH-3012 Bern, Switzerland
e-mail: peter.peier@iap.unibe.ch

K.A. Nelson
Department of Chemistry, MIT, Cambridge, MA 02139, USA

tion by a second time-delayed visible probe pulse [23, 24]. The frequency as well as the wave vector spectrum of the THz waves are dominated by the spatial properties of the driving laser, offering the possibility to tailor both within some limits. Specifically, by focusing the driving laser to a narrow line at the nonlinear crystal, an almost plane single-cycle wavepacket with an angular spread of less than half a degree is generated. Thus, tunneling of single-cycle pulses can be imaged and investigated under well-controlled conditions. Moreover, our detection scheme is unique in the sense that it allows for a very precise spatial and temporal measurement of the THz electric field distribution before and after tunneling. Thus, it is possible to separate effects due to tunneling from those due to propagation in the bulk crystals. We compare our measurements with analytic results following the analysis outlined in reference [16]. Our results corroborate the findings in [17]; however, the analysis is somewhat easier since we visualize the THz wave before and after tunneling through the barrier. Specifically, the effects due to propagation and tunneling can be separated.

2 Theoretical considerations

In the following sections we outline the fundamentals to fully describe tunneling of THz waves, which includes phonon–polariton generation, tunneling itself, and phonon–polariton detection.

2.1 Generation of THz phonon–polaritons

When an intense laser pulse $\boldsymbol{\mathcal{E}}(\mathbf{r},\omega)$ passes through a $LiNbO_3$ crystal it creates a nonlinear polarization which may act as a source term for a THz field $\mathbf{E}(\mathbf{r},\omega)$ [20, 21]

$$\nabla^2\mathbf{E}(\mathbf{r},\omega)+\frac{\omega^2}{c^2}\epsilon(\omega)\mathbf{E}(\mathbf{r},\omega) = -\frac{\omega^2}{c^2}\chi^{(2)}\boldsymbol{\mathcal{E}}(\mathbf{r},\omega)\otimes_\omega\boldsymbol{\mathcal{E}}^*(\mathbf{r},\omega), \tag{1}$$

where c is the speed of light in vacuum, $\chi^{(2)}$ the effective second order nonlinearity, which includes electronic and ionic contributions, and $\otimes_\omega$ the convolution with respect to frequency. In the low-frequency limit, i.e. $\epsilon(\omega)\approx\epsilon(0)$, the above equation is easily Fourier transformed to give

$$\nabla^2\mathbf{E}(\mathbf{r},t)-\frac{\epsilon(0)}{c^2}\frac{\partial^2\mathbf{E}(\mathbf{r},t)}{\partial t^2}=\frac{1}{c^2}\chi^{(2)}\frac{\partial^2}{\partial t^2}|\mathcal{E}(\mathbf{r},t)|^2. \tag{2}$$

This differential equation is formally solved by the Green function method provided that the excitation field is known.

In all experiments following, the excitation source is a y-polarized laser pulse with a wave vector $\mathbf{k}_{\text{pump}}\|x$ which is focused to a line parallel to the y-axis as shown in Fig. 1(a).

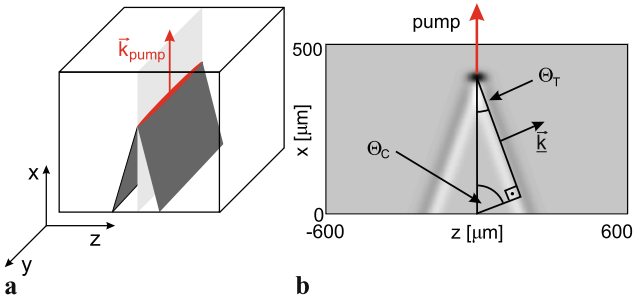

Fig. 1 (**a**) The laser pulse is focused to a line, propagates in the upward direction, and generates two nearly plane THz wavelets propagating almost perpendicular to the direction of the laser pulse. (**b**) The THz response generated at the front surface has traveled some distance before the excitation pulse reaches the back of the sample. If the THz source moves faster than the phase velocity of the THz radiation generated, the THz field can be thought of Cherenkov-type radiation

The optic axis of the $LiNbO_3$ crystal is parallel to the y-axis and so is the THz electric field vector. If we assume that the excitation field is an infinitely tall line source which moves parallel to the x-axis without changing its shape, the 2D Green function in the x–z plane is [21]

$$G_{2D}(x,z,t)=\frac{2\pi}{\epsilon_0\tan\theta_C}\mathrm{H}\big(v_{\mathrm{gr}}t-x-|z|\tan\theta_C\big), \tag{3}$$

where H is the Heaviside step function, v_{gr} the group velocity of the driving laser pulse, $\tan\theta_{\mathrm{C}}=\sqrt{(nv_{\mathrm{gr}}/c)^2-1}$, and $n=\sqrt{\epsilon(0)}$ the index of refraction of $LiNbO_3$ at THz frequencies. If we further assume that the excitation field has a Gaussian spatial profile of width w_0 in the z-dimension and a Gaussian temporal profile of duration τ, the 2D solution is an almost plane single-cycle wavelet given by

$$E_y(x,z,t)\propto\frac{\partial}{\partial x}\int \mathrm{d}z'\,\mathrm{e}^{-2z'^2/w_0^2} \times\exp\left[-\frac{(x-v_{\mathrm{gr}}t+|z-z'|\tan\theta_{\mathrm{C}})^2}{v_{\mathrm{gr}}^2\tau^2}\right]. \tag{4}$$

A solution to (4) is shown in Fig. 1(b). The laser pulse propagates in the upward direction and has traveled about 400 µm into the crystal. The THz response generated near the front surface has traveled some measurable distance before the excitation pulse reaches the back of the sample and generates a THz field there. Because the radiation source moves faster than the phase velocity of the radiation generated, the THz field can be thought of Cherenkov-type radiation as indicated in Fig. 1(b) [20–22]. For $LiNbO_3$ the Cherenkov angle θ_{C} is 64 degrees. Frequently, we use the term tilt angle of the THz wavefront, which is given by $\theta_{\mathrm{T}}=90-\theta_{\mathrm{C}}$. Figure 1(b) also shows that the temporal profile of the THz wavelet is that of a single-cycle pulse with a central carrier frequency in the THz range and pulse duration on the order of a few ps. The pulse duration is roughly

determined by the spatial derivative of the driving laser's transverse spatial profile with respect to z, and the carrier frequency may be estimated to $f_c \approx \frac{c}{\pi n w_0}$ [25]. That is, by changing the pump beam waist w_0, the central carrier frequency and the bandwidth of the THz pulse can be varied. In the low-frequency range, where our experiments are performed, most of the THz phonon–polariton energy is in the radiation field.

2.2 Tunneling of THz phonon–polaritons

Once the THz phonon–polariton encounters a crystal–air interface, the angle of incidence determines whether it is partially transmitted and reflected or whether it undergoes total internal reflection. For $LiNbO_3$ the critical angle is only $\theta_{TIR} = 11.28$ degrees, that is, the THz waves shown in Fig. 1(b) are totally reflected at the back surface as well as at the side surfaces of the crystal. The angle of incidence at the side surfaces coincides with the tilt angle θ_T. When a second crystal is placed to the right of the first crystal, with the air gap separating the two crystals on the order of a wavelength, tunneling occurs, as shown in Fig. 2(a). Part of the THz wave is reflected and the rest tunnels through the gap.

Tunneling through the air gap is best described by decomposing the incident wavepacket into a superposition of plane waves and by applying the appropriate linear transfer function to every plane wave before reconstructing the wavepacket in the second crystal. In order to derive the linear transfer function we consider the geometry depicted in Fig. 2(b). The two crystals, which are separated by an air gap of width d, define three different regions of interest. Each THz plane wave component travels from the left to the right with a wave vector $\mathbf{k}$ and impinges on the first crystal–air interface at an angle of incidence θ. The total field to the left of the air gap consists of an incident plane wave $E_y^{\mathrm{i}}(x,z,t)$ and a reflected plane wave $E_y^{\mathrm{r}}(x,z,t)$. In the air gap the field is composed of two exponentially decaying waves $E_y^{+}(x,z,t)$ and $E_y^{-}(x,z,t)$. To the right of the air gap there is only the transmitted plane wave $E_y^{\mathrm{t}}(x,z,t)$. This Ansatz very closely follows reference [16] for TE polarization, that is, the electric field has a y component only, whereas the magnetic field has an x and a z component. We write the electric fields in the different regions as

$$E_y^{\mathrm{i}}(x,z,t) = E_0 \exp\big[-i\omega t + ik_0 n(\alpha x + \gamma z)\big], \tag{5}$$

$$E_y^{\mathrm{r}}(x,z,t) = \rho E_0 \exp\big[-i\omega t + ik_0 n(\alpha x - \gamma z)\big], \tag{6}$$

$$E_y^{+}(x,z,t) = p E_0 \exp\big[-i\omega t + ik_0 (n\alpha x + i\Gamma z)\big], \tag{7}$$

$$E_y^{-}(x,z,t) = m E_0 \exp\big[-i\omega t + ik_0 (n\alpha x - i\Gamma z)\big], \tag{8}$$

$$E_y^{\mathrm{t}}(x,z,t) = \tau E_0 \exp\big[-i\omega t + ik_0 n\big(\alpha x + \gamma (z-d)\big)\big], \tag{9}$$

with $k_0 = \omega/c$, $\Gamma = \sqrt{n^2 - 1 - n^2\gamma^2} > 0$, $\gamma = \cos\theta$, and $\alpha = \sin\theta$. From the electric field we can derive the magnetic field through Maxwell's equations and with the continuity of the tangential field components a system of four equations results, defining the reflection and transmission coefficients

$$1 + \rho = p + m, \tag{10}$$

$$\tau = p \exp(-k_0 \Gamma d) + m \exp(k_0 \Gamma d), \tag{11}$$

$$in\gamma(1-\rho) = -\Gamma(p-m), \tag{12}$$

$$in\gamma\tau = -\Gamma\big[p \exp(-k_0\Gamma d) - m \exp(k_0 \Gamma d)\big]. \tag{13}$$

Throughout the remainder of this publication the emphasis is on the transmitted part of the wavelet. Thus, the only coefficient of interest is the transmission coefficient τ which is found to be

$$\tau = i \frac{4n\gamma\Gamma}{n^2\gamma^2 + \Gamma^2} \frac{1}{\exp(k_0\Gamma d + 2i\phi) - \exp(-k_0\Gamma d - 2i\phi)}, \tag{14}$$

with $\phi = \arctan(\Gamma d/c)$. Given the transmission coefficient for each plane wave constituting the THz wavelet, the transmitted wavelet after tunneling through the air gap is

$$E_y^{\mathrm{t}}(x,z,t) \propto \int_{-\infty}^{\infty} \mathrm{d}\omega\, \tau(\omega) E_0(\omega) \times \exp\big[-i\omega t + ik_0 n\big(\alpha x + \gamma(z-d)\big)\big], \tag{15}$$

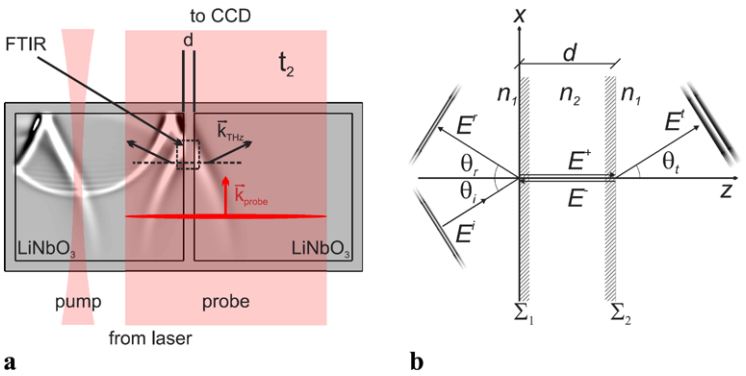

Fig. 2 (**a**) Electric field distribution of the THz waveform some time after the excitation pulse has passed through the left crystal. The probe pulse illuminates part of the *left* and most of the *right* crystal. (**b**) Detailed sketch indicating the three different regions of interest and the electric fields therein together with their wave vectors

with $E_0(\omega)$ being the amplitude in the frequency domain of the incident wavepacket. From the transmission coefficient we derive the traversal time for the phase of each plane wave traveling the distance γd as

$$t_{\mathrm{ph}} = \frac{\arg(\tau)}{\omega} = \frac{1}{\omega}\arctan\left[\frac{n^2\gamma^2 - \Gamma^2}{2n\gamma\Gamma}\tanh(k_0\Gamma d)\right]. \quad (16)$$

For a wavepacket consisting of plane waves with different frequencies but having the same direction of propagation, the group delay is

$$t_{\mathrm{gr}} = \frac{\partial\arg(\tau)}{\partial\omega} = \frac{2n\gamma\Gamma(n^2\gamma^2 - \Gamma^2)\,\Gamma d/c}{(2n\gamma\Gamma)^2\cosh^2(k_0\Gamma d) + (n^2\gamma^2 - \Gamma^2)^2\,\sinh(k_0\Gamma d)}. \quad (17)$$

2.3 Detection of phonon–polaritons

The propagating THz phonon–polaritons locally change the material's index of refraction through the electro-optic effect. That is, a probe pulse illuminating the second crystal some time after the pump has passed through will experience a locally varying phase modulation which is proportional to the electric field of the THz wavelet. When pump and probe pulse have the same wavelength, then the probe pulse 'surfs' on the THz wave [20] and the phase modulation is independent of x. If the probe pulse is also polarized along the y direction, its spectral components will be modulated according to

$$\mathcal{E}_y(D, y, z, \omega, \Delta t) = \mathcal{E}_y(0, y, z, \omega)\mathrm{e}^{-ik(y,z,\omega,\Delta t)D} \quad (18)$$

where Δt is the time delay between pump and probe pulse and D is the thickness of the crystal. We have

$$k(y, z, \omega, \Delta t) = \frac{\omega}{c}\left[n_e - \frac{n_e^3}{2}r_{33}E_y(x = 0, y, z, \Delta t)\right]. \quad (19)$$

Note that for our excitation geometry the THz wave $E_y(x = 0, y, z, \Delta t)$ has no y dependence, in other words, the phase modulation is a function of z and Δt only. Assuming $\omega \approx \omega_0$ with the probe pulse carrier frequency ω_0 and frequency independent indices of refraction, and further assuming an initially uniform transverse probe beam profile, one finds after Fourier transformation to the time domain

$$\mathcal{E}_y(D, z, t, \Delta t) = \mathcal{E}_y(t)\mathrm{e}^{-ik(z,\Delta t)D}, \quad (20)$$

with

$$k(z, \Delta t) = \frac{\omega_0}{c}\left[n_e - \frac{n_e^3}{2}r_{33}E_y(z, \Delta t)\right]. \quad (21)$$

The phase modulation of the probe pulse integrated through the crystal thickness $\phi_D = k(z, \Delta t)D$ can be measured through interferometry. Here, we use a Sagnac interferometer where the reference beam passes through the crystal before a THz wavelet is generated and experiences a constant phase modulation $\phi_0 = \omega_0 n_e D/c$. Thus, the interference pattern measured by a CCD camera is given by

$$I(z, \Delta t) \propto \int_{-\infty}^{\infty} \mathrm{d}t\left|\mathcal{E}_y(t)\right|^2 \times \left|\exp\left[-i\phi_D(z, \Delta t)\right] + \exp\left[-i\phi_0 - i\xi(z)\right]\right|^2 \propto 1 + \cos\left[\phi_D(z, \Delta t) - \phi_0 - \xi(z)\right], \quad (22)$$

where we allow for an additional phase shift $\xi(z)$ of the reference pulse. Ideally, one chooses a constant phase shift of a quarter wavelength, i.e. $\xi(z) = \pi/2$, in which case the measured intensity is proportional to the THz electric field $E_y(z, \Delta t)$ (assuming $\phi_D(z, \Delta t) - \phi_0 \ll 1$). Alternatively, the reference pulse may be tilted, i.e. $\xi(z) = \xi_0 z$, with ξ_0 determining the tilt angle, and some Fourier processing is required to extract the THz electric field. Since the interference pattern is uniform along the y-axis we can integrate the measured CCD images along the y-axis and thereby improve the signal-to-noise ratio. Throughout the remainder of this publication we will present such 1D display of the THz electric fields, i.e. $E_y(z, \Delta t)$.

3 Experimental

The intense laser pulses originate from a kHz Ti:sapphire multi-pass amplifier and have a pulse duration of approximately 100 fs. Part of the laser output is focused with a cylindrical lens to a line on the first $LiNbO_3$ crystal and generates the two counter-propagating THz wavelets. A smaller, time-delayed part of the laser pulses is directed to a Sagnac interferometer; the time delay Δt is adjusted through a motorized delay stage. The $LiNbO_3$ crystal is located close to the beam splitter of the Sagnac interferometer and is imaged onto a CCD camera. Due to this asymmetry, the reference pulse passes through the crystal about 1 ns before the probe pulse. Details about the detection setup can be found in reference [24]. In order to investigate the transmitted field as a function of the tunneling distance, we have variably displaced the crystal to the left together with the pump beam (see Fig. 2). The position of the right crystal and the alignment of the probe path were not changed, and the time delay between pump and probe was the same for all measurements. By moving the pump beam together with the left crystal, we ensure that the THz wave always travels the same distance within the crystalline material, irrespective of the air gap width, and we avoid any waveform reshaping due to THz dispersion in the crystal.

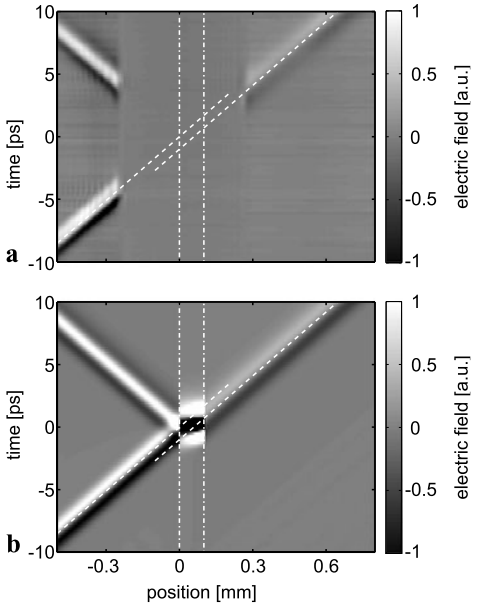

Fig. 3 Space-time *gray* scale images showing the incident and the reflected THz pulses to the *left* of the air gap and the transmitted THz pulse to the *right* of the air gap. The *gray* scale is proportional to the electric field amplitude. (**a**) Experimental and (**b**) theoretical results

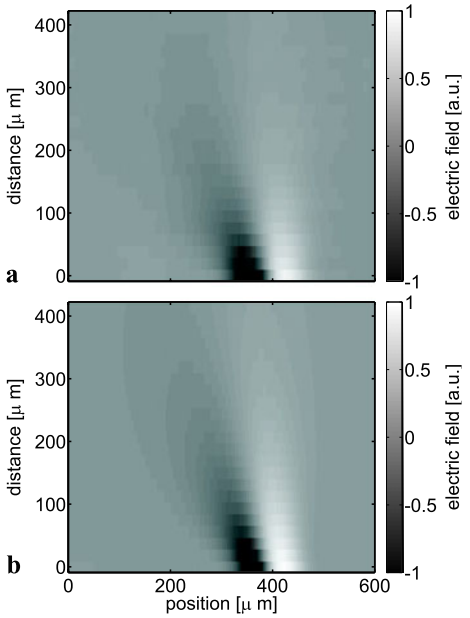

Fig. 4 Experimental (**a**) and calculated (**b**) time domain THz waveforms as a function of position and air gap width. The *gray* scale indicates the electric field strength

4 Results and discussion

Figure 4(a) shows a space-time plot of the THz wave tunneling through a 100 μm wide air gap. The gray scale image is comprised of a series of measurements of the spatial THz field distribution at different pump–probe time delays $E_y(z, \Delta t)$ which have been stacked on top of each other so that time runs along the vertical axis. The gray scale is proportional to the THz electric field amplitude.

The incident single-cycle THz wave starts at the far left side of the crystal on the left and propagates rightward toward the air gap as time progresses. Its most prominent features in Fig. 3(a), i.e. maximum, minimum or zero crossing, fall along a straight line with a slope that is determined by the inverse of the phase velocity in $LiNbO_3$. Part of the THz wave is reflected at the first crystal–air interface and propagates in the opposite direction. The remaining part of the THz wave tunnels through the air gap and appears in the second crystal on the right where it propagates farther rightward. The origin has been arbitrarily shifted to the left side of the air gap and to the time when the incident THz pulse arrives at this point. The area around the air gap could not be imaged because of probe light being scattered at the crystals edges. Nevertheless, the agreement between experimental results and the calculations is excellent and a few interesting details can be inferred from Fig. 3. First, a comparison between a horizontal lineout of the incident and the reflected THz wave shows that the reflected THz wave acquires a phase shift of $\pi/2$ upon total internal reflection (single-cycle shaped becomes Mexican-hat shaped). Second, the offset between the light lines of the incident and the transmitted THz waves implies that the pulses bridge the air gap with a group velocity that is faster than the group velocity in $LiNbO_3$. In order to determine the exact speed we have examined the transmitted waveform after tunneling through the air gap in more detail. Figure 4(a) shows a series of those waveforms $E_y(z, \Delta t)$ for increasing air gap width, which are stacked on top of each other resulting in a 2D intensity plot with the gray scale being proportional to the electric field amplitude. The air gap and the first crystal are to the left of the image and distances are measured with respect to the edge of the detection crystal.

Comparing the experimental results in Fig. 4(a) to the calculations in Fig. 4(b), which are based on (15), shows excellent agreement. The input THz field $E_0(\omega)$ in (15) was approximated by a suitable analytic expression based on the experimentally measured temporal profile $E_0(t)$. A reasonable choice is $E_0(t) \propto t \exp(-t^2/\sigma_t^2)$ and with the pulse duration σ_t obtained from a fit to the incident waveform. As the air gap width increases, the THz waveform decays rapidly in amplitude and broadens considerably in time. In addition to the reshaping, the THz waveform is displaced towards negative distances which is a result of the tunneling geometry and will be discussed in more detail in the following. The exponential decay is best analyzed by Fourier transforming the time domain signals to the frequency domain as shown in Fig. 5(a).

We first extract the wave vector spectrum through a Fourier transformation of $E_y(z, \Delta t)$ with respect to z. Thereafter, we use the dispersion relation of $LiNbO_3$ to con-

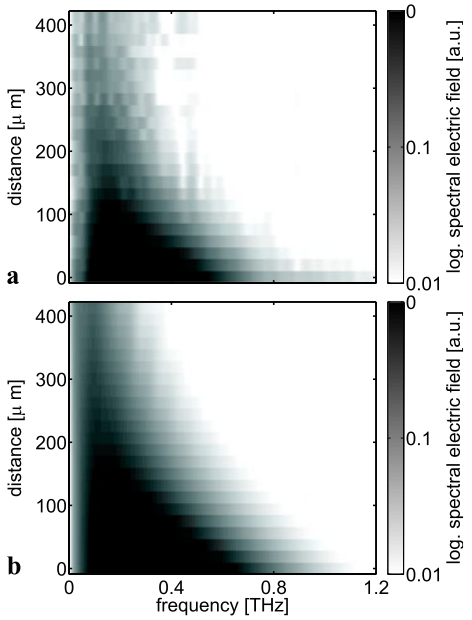

Fig. 5 Logarithmic plot of (**a**) the measured and (**b**) the calculated spectral amplitude as a function of air gap width. The *gray* scale is proportional to the logarithm of the spectral amplitude

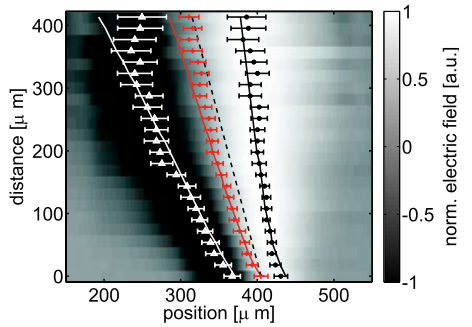

Fig. 6 Measured THz waveforms as a function of position and air gap width. For each air gap width the electric field amplitudes were normalized. The symbols indicate the positions of the minima (*white triangles*), the zero crossings (*red ticks*), and the maxima (*black circles*). The *solid lines* result from the analytic expressions given above and the *dashed line* indicates the *light line*

vert the wave vector axis to a frequency axis. Given the good agreement between the experimental results and the calculations of the THz waveforms in Fig. 4, it is not surprising that the measured and the calculated spectral amplitudes coincide very well. The low-pass characteristics of the transfer function describing the tunneling process can be readily seen. With increasing air gap width, more and more high-frequency components disappear and the carrier frequency effectively shifts to lower values. In order to better visualize the reshaping process, the data presented Fig. 4 are normalized so that all THz waveforms have the same amplitude. The resulting field distribution is shown in Fig. 6.

The white triangles mark the positions of the minima, the red ticks the positions of the zero crossings, and the black circles the positions of the maxima. The solid lines are derived from (16), and the agreement with the measured data is very good. Deviations appear at large tunneling distances, but here the signal is close to the noise floor and determination of the minima, maxima et cetera becomes increasingly difficult. As pointed out in reference [17] it is not possible to calculate the group velocity because the path through the tunnel barrier is unknown when decomposing the THz wavepacket into a superposition of plane waves. Given the small angular spread of the THz wavepacket in the present experiments we may neglect the spatial wave vector distribution and assume a purely temporal wavepacket, that is, a wavepacket composed of plane waves with different frequencies but with the same wave vector. In this case we find the phase and the group delay for a wavepacket traveling the distance γd through the tunnel barrier given by (16) and (17). In addition to the phase delay we can determine the time delays for the minima and maxima of the THz wavepacket as shown in Fig. 4. The dashed line indicates the position of the zero crossing if it would tunnel the same distance through the air gap with the speed of light in vacuum. Upon comparison we find that only the position of the maxima seems to propagate with a super-luminal velocity, however, this is due to the low-pass characteristic of the tunneling process rather than a super-luminal velocity.

5 Conclusion

We have visualized amplitude and phase modulations in tunneling of single-cycle THz waves through spatiotemporal imaging of the electric field distribution before and after tunneling which allows us to disentangle effects due to tunneling from those due to propagation in the bulk crystals. The THz wavepackets undergo strong reshaping because of the low-pass characteristic of the tunneling process. All experimental observations can be fully understood on the basis of a causal linear dispersion theory.

Acknowledgement This work was funded by the Swiss National Science Foundation under project number 200020-119934.

References

1. F. Hund, Z. Phys. **43**, 805 (1927)
2. G. Gamow, Z. Phys. **51**, 204 (1928)
3. Th. Martin, R. Landauer, Phys. Rev. A **45**, 2611 (1992)
4. R.Y. Chiao, A.M. Steinberg, in *Progress in Optics*, vol. 37, ed. by E. Wolf (Elsevier, Amsterdam, 1997), p. 345
5. E.E. Hall, Phys. Rev. **15**, 73 (1902)
6. R.W. Astheimer, G. Falbel, S. Minkowitz, Appl. Opt. **5**, 87 (1966)
7. A.R. Afshar, A. Thetford, Eur. J. Phys. **3**, 72 (1982)

8. E.H. Hauge, J.A. Støvneng, Rev. Mod. Phys. **61**, 917 (1989)
9. R. Chiao, arXiv:quant-ph/9811019v1 [quantum physics] (1998)
10. H.G. Winful, Phys. Rep. **436**, 1 (2006)
11. J.J. Carey, J. Zawadzka, D.A. Jaroszynski, K. Wynne, Phys. Rev. Lett. **84**, 1431 (2000)
12. A.M. Steinberg, P.G. Kwiat, R.Y. Chiao, Phys. Rev. Lett. **71**, 708 (1993)
13. A.M. Steinberg, R.Y. Chiao, Phys. Rev. A **49**, 3283 (1994)
14. V.L. Brudny, Opt. Exp. **9**, 561 (1994)
15. A. Ranfagni, D. Mugnai, P. Fabeni, G.P. Pazzi, G. Naletto, C. Sozzi, Physica B **175**, 283 (1991)
16. D. Mugnai, A. Ranfagni, L. Ronchi, arXiv:physics/0111192v1 [physics.optics] (1998)
17. M.T. Reiten, D. Grischkowsky, R.A. Cheville, Phys. Rev. E **64**, 036604 (2001)
18. M.T. Reiten, K. McClatchey, D. Grischkowsky, R.A. Cheville, Opt. Lett. **26**, 1900 (2001)
19. K. Wynne, J.J. Carey, J.Z. Zawadzka, D.A. Jaroszynski, Opt. Commun. **176**, 429 (2000)
20. D.H. Auston, M.C. Nuss, IEEE J. Quantum Electron. **24**, 184 (1988)
21. D.H. Auston, K.P. Cheung, J.A. Valdmanis, D.A. Kleinman, Phys. Rev. Lett. **53**, 1555 (1984)
22. J.K. Wahlstrand, R. Merlin, Phys. Rev. B **68**, 054301 (2003)
23. T. Feurer, N.S. Stoyanov, D.W. Ward, J.C. Vaughan, E.R. Statz, K.A. Nelson, Ann. Rev. Mater. Res. **37**, 317 (2007)
24. P. Peier, S. Pilz, F. Müller, K.A. Nelson, T. Feurer, J. Opt. Soc. Am. B **25**, 70 (2008)
25. T. Feurer, J.C. Vaughan, T. Hornung, K.A. Nelson, Opt. Lett. **29**, 1802 (2004)